JGR Planets

RESEARCH ARTICLE
10.1029/2022JE007598

Special Section:
The Mars Perseverance Rover Jezero Crater Floor Campaign

RIMFAX Ground Penetrating Radar Reveals Dielectric Permittivity and Rock Density of Shallow Martian Subsurface

T. M. Casademont[1], S. Eide[1], E. S. Shoemaker[2], Y. Liu[3], D. C. Nunes[3], P. Russell[4], H. Dypvik[1], H. E. F. Amundsen[1], T. Berger[1], and S.-E. Hamran[1]

[1]Centre for Space Sensors and Systems, University of Oslo, Kjeller, Norway, [2]Lunar and Planetary Laboratory, University of Arizona, Tucson, AZ, USA, [3]Jet Propulsion Laboratory, California Institute of Technology, Pasadena, CA, USA, [4]Earth, Planetary and Space Sciences, University of California, Los Angeles, Los Angeles, CA, USA

Key Points:

- First detailed dielectric permittivity and bulk rock density measurements of the shallow Martian subsurface with ground penetrating radar are presented
- Permittivities and densities are consistent with a solid-rock, mafic subsurface
- Permittivities are in the range of Mars orbital radar results; densities compare with surficial densities from other Rover instruments

Supporting Information:

Supporting Information may be found in the online version of this article.

Correspondence to:

T. M. Casademont,
titus.casademont@its.uio.no

Citation:

Casademont, T. M., Eide, S., Shoemaker, E. S., Liu, Y., Nunes, D. C., Russell, P., et al. (2023). RIMFAX ground penetrating radar reveals dielectric permittivity and rock density of shallow Martian subsurface. *Journal of Geophysical Research: Planets*, *128*, e2022JE007598. https://doi.org/10.1029/2022JE007598

Received 3 OCT 2022
Accepted 15 MAR 2023
Corrected 2 JUN 2023

This article was corrected on 2 JUN 2023. See the end of the full text for details.

Author Contributions:

Conceptualization: T. M. Casademont, S. Eide, S.-E. Hamran
Data curation: T. Berger
Formal analysis: T. M. Casademont

Abstract The Mars 2020 Perseverance Rover is equipped with the RIMFAX ground penetrating radar instrument which has been continuously surveying the shallow subsurface during the rover's journey. Within the first 379 mission days, we identify hyperbolic patterns in the data, which are thought to be caused by objects such as buried boulders or cavities located in the upper 5 m of the subsurface. To obtain the first detailed estimates of radar wave propagation velocity, we match these scatterer-generated patterns with theoretical traveltime hyperbolas, which take into account the refraction at the surface. We employ these estimates to derive the average dielectric permittivity and bulk rock density of the volume above the scatterer source. The parameters compare well with those obtained through orbital radar measurements and those measured by other instruments onboard the Perseverance Rover. Our findings are consistent with a subsurface dominated by solid rock and mafic material.

Plain Language Summary The Mars 2020 Perseverance Rover carries the RIMFAX instrument, the first ground-penetrating radar on a NASA Mars rover. It continuously transmits radar waves into the subsurface while the Rover moves and records the reflected echoes to create images of the subsurface and determine material properties. Here, we use arch-shaped patterns in the data to find out about the dielectric permittivity and rock density. Both properties match well with estimates from other instruments onboard the Perseverance Rover and from Mars orbiters. Our findings indicate a solid-rock subsurface composed of volcanic material.

1. Introduction

The Mars Rover Perseverance is the first NASA Rover with a ground penetrating radar (GPR) payload, the "Radar Imager for Mars' Subsurface Experiment" (RIMFAX) (Hamran et al., 2020). RIMFAX has continuously sounded the upper tens of meters of the Martian subsurface along the Rover traverse, taking the first in situ observations of the shallow Martian subsurface with its long microwave penetration. In this study, we analyze the first 8 km of data, starting at the Octavia E. Butler landing site, where Perseverance landed on 18 February 2021 (see Figure 1 for a map of the landing site and Rover traverse).

Numerous studies with Perseverance instruments have classified the overall surficial geology and mineralogy as igneous (e.g., Farley et al., 2022; Liu et al., 2022; Wiens et al., 2022). The study area is then characterized by the two major formations, Máaz Fm and Séítah Fm. For Máaz Fm, Udry et al. (2022) propose the material to be deposited by different lava flows or less likely pyroclastic flows. Its composition is basaltic to basaltic-andesitic. Spectral variability and morphology of Máaz-outcrops lead to further distinction of the Máaz-subregions, upper and lower Máaz, encompassing the eastern, respectively, southern part, with a transitional zone around the south-eastern tip of Séítah (Horgan et al., 2022). In contrast to Máaz, Séítah is interpreted as an olivine cumulate formed by slow cooling magma (Liu et al., 2022; Wiens et al., 2022). On average, Wiens et al. (2022) found less olivine and lower density in Máaz than Séítah. For the emplacement scenario they proposed either olivine settling in a common cumulate spanning Séítah and Máaz or separate lava flows for Máaz with respective erosional contrasts below. Based on radar reflections, Hamran et al. (2022) show that Séítah is the lowermost stratigraphic unit in the studied area, with Séítah horizons dipping under Máaz in multiple locations in the vicinity of the visible surface boundary between the two formations.

Funding acquisition: S.-E. Hamran
Investigation: T. M. Casademont
Methodology: T. M. Casademont, S.-E. Hamran
Project Administration: T. Berger, S.-E. Hamran
Resources: T. M. Casademont
Software: T. M. Casademont
Supervision: S.-E. Hamran
Validation: T. M. Casademont
Visualization: T. M. Casademont, S. Eide
Writing – original draft: T. M. Casademont, E. S. Shoemaker, Y. Liu
Writing – review & editing: T. M. Casademont, S. Eide, E. S. Shoemaker, D. C. Nunes, P. Russell, H. Dypvik, H. E. F. Amundsen

In this study, we present estimates of subsurface rock parameters within the Máaz and Séítah formations with horizontal resolution of a few meters and up to 5 m depth, as measured by GPR. The fundamental analyzed parameter is the radar wave propagation velocity. The velocity is needed to estimate the depth and height of subsurface features such as the height and dipping angle of buried stratigraphy. Further image enhancement such as geophysical migration rely on a realistic velocity model of the subsurface. Furthermore, for dry and nonmagnetic material, the velocity is interchangeable with the real part of the relative dielectric permittivity (hereafter "permittivity"). The later can then be related to the bulk rock density (hereafter "density") based on empirical relationships. Both permittivity and density help to constrain the subsurface material and bulk consistency, and therefore contribute to determining the geologic composition of the Jezero Crater floor subsurface. Another governing material parameter in this context is the radar wave attenuation, which is analyzed for this study area by Eide, Casademont, Berger, et al. (2022) and is not regarded here.

To ensure comparability, we present our findings in the permittivity domain rather than velocity, since the permittivity of Martian shallow subsurface has been measured from orbit by the Shallow Radar (SHARAD) and Mars Advanced Radar for Subsurface and Ionospheric Sounding (MARSIS). From orbit, the permittivity can be determined in regions where an independent measurement of the thickness of a particular layer is available. SHARAD (20 MHz center frequency) and MARSIS (1.8, 3, 4, and 5 MHz sounding modes) have estimated the permittivity of layers within the polar ice caps, buried ice deposits across Mars, and that of dry rocky materials such as lava flows and pyroclastic deposits (e.g., Carter, Campbell, Holt, et al., 2009; Carter, Campbell, Watters, et al., 2009; Ganesh et al., 2020; Shoemaker et al., 2022; Simon et al., 2014; Watters et al., 2007). Given the suggested igneous surface material of Jezero, the orbital permittivity studies for lava flows on Mars are most relevant for comparison with RIMFAX findings. The thicknesses of basaltic lava flows near Ascraeus Mons in the Tharsis Volcanic Province were measured and permittivity was inferred to range from 6.2 to 17.3 and later reestimated to range from 7.6 ± 2.3 to 11.6 ± 4.2 with an average of 9.6 (Carter, Campbell, Holt, et al., 2009; Simon et al., 2014). Another study used additional SHARAD coverage to refine this range from 7 to 11.2 with an average of 9.7, using a different methodology to infer flow thickness (Shoemaker et al., 2022). These orbital measurements are in good agreement with the permittivity of terrestrial, laboratory derived values: dense, dry, and basaltic lava flows appear to range between 7 and 11, while for pyroclastic material (i.e., ash and tephra), the permittivity is found to be as low as 3 (Campbell & Ulrichs, 1969; F. Ulaby et al., 1990). Laboratory analysis of Martian analog samples by Stillman and Olhoeft (2008) also show that both permittivity and loss tangent can be temperature-dependent. In particular, their gray hematite samples show dielectric relaxation frequencies in the lower RIMFAX band for temperatures around 200 K, yet their experiments only cover the lowest RIMFAX frequencies. For other samples like olivine and plagioclase, they do not find a temperature dependence to be significant within the uncertainty and frequency range of our study. While the materials of Stillman and Olhoeft (2008) have been found in Jezero Crater rocks (e.g., Farley et al., 2022; Horgan et al., 2022; Wiens et al., 2022), the temperature-independent substances are the more abundant. Therefore, we consider temperature effects to be negligible for the purposes of this work.

In this study, we quantify the subsurface radar wave propagation velocity in Jezero Crater by adapting the hyperbola matching technique for the surface refraction occurring for air-lifted GPRs in Section 2. In Section 3, we analyze the derived permittivity and density distributions and confine the material by literature comparison. Subsequently we correlate our results to densities of surficial rocks as seen by different Rover instruments in Section 4.

2. Method

RIMFAX is a monostatic frequency modulated continuous wave (FMCW) radar with a sawtooth modulated frequency sweep. The frequency range is 150 Mhz to 1.2 GHz, that is a free-space wavelength of 2–0.25 m. The free-space vertical resolution is 0.15 m. For a detailed instrument description, see Hamran et al., 2020. RIMFAX differs from many Earth-based industrial GPRs most notably by the FMCW signal and the antenna feed point elevation of 0.75 m above ground. The elevation in free air has to be considered, since it leads to refraction at the air-surface boundary, effectively inward refracting rays (i.e., steepening) into the subsurface (Pue et al., 2016).

2.1. Hyperbola Matching in Layered Model

The permittivity is related to the radar wave propagation velocity v by

$$v = c/\sqrt{\varepsilon'}, \quad (1)$$

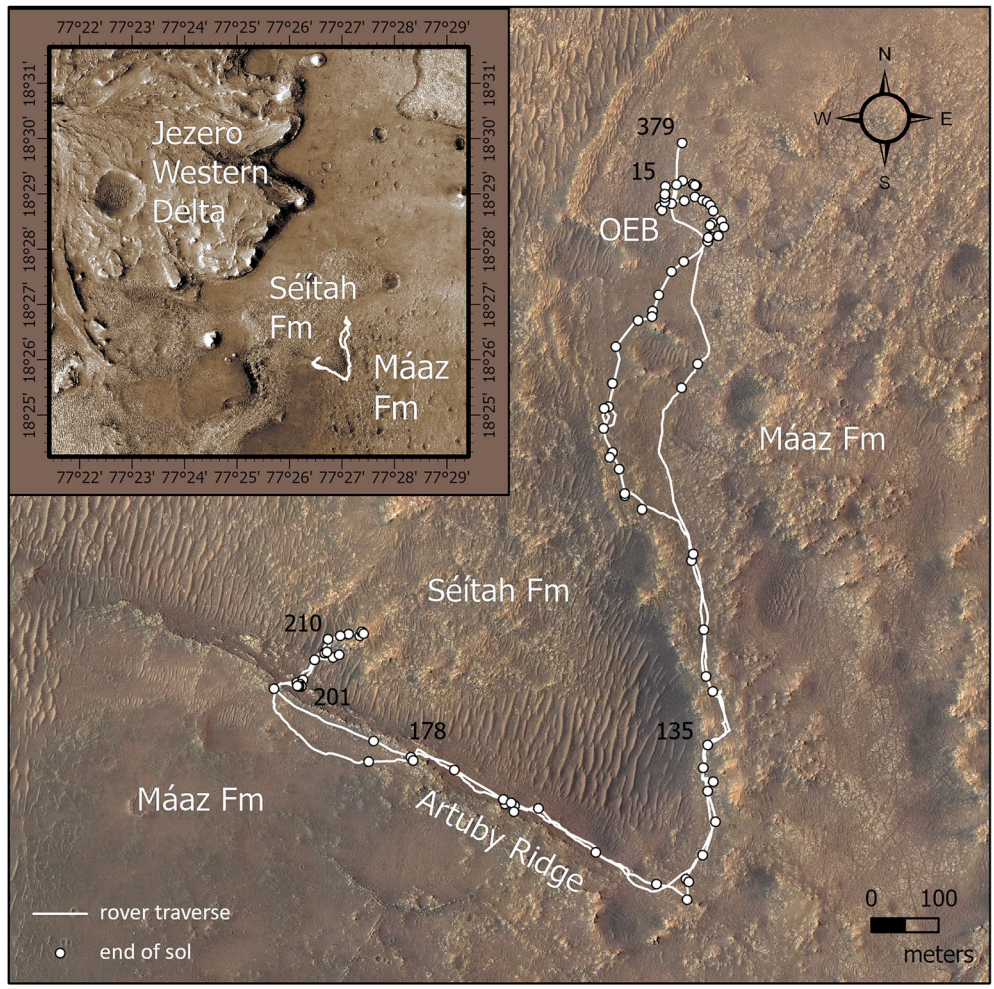

Figure 1. Rover path from the first drive sol 15 from Octavia E. Butler landing site (OEB) until sol 379, traversing the formations Máaz and Séítah and reverse. End of drive (eod) locations marked with white dots. Basemap: Mars 2020 Science Team RGB-colored HiRISE mosaic.

assuming a dry, nonmagnetic and low-loss medium. The velocity can be derived by the hyperbola matching technique, leading to permittivity and consequently density. Classical hyperbola matching is a widely used technique in Earth-based GPR applications. It estimates the average velocity above a buried scatterer by fitting the theoretical two-way traveltime (twt) curve $t(x) = \sqrt{x^2 + y^2}/v$ to the hyperbolic shape in the data, with lateral antenna offset x from the scatterer, scatterer depth y, and velocity v. The twt curve is based on the high-frequency limit for ray optics, assuming that the dispersive nature of soil and rocks is negligible and the velocity is considered constant over the radar bandwidth. The scatterer is considered to be a point-like object. Generally, scattering from point-like objects produces weaker returns as opposed to extended structures like layers due to the geometric spreading of the energy over larger volumes (Schwarz, 2019).

Classical hyperbola matching has also been used on the Chinese Chang'E 3 and 4 missions as a primary source of velocity determination of the subsurface (Dong, Feng, Zhao, et al., 2020; Dong, Fang, Zhou, et al., 2020; Feng et al., 2017; Lai et al., 2016, 2019; Li & Zhang, 2021; Li et al., 2020). The classical hyperbola matching as used therein does not account for the air-layer between antenna and ground, which can be several decimeters in case of rover-mounted antennas. In such an air-layer scenario, the refraction at the air-surface interface with a strong impedance contrast has to be taken into account. Geometric rays from the antenna to the scatterer are no longer straight lines. The angle of refraction depends on the contrast in refractive indices and is governed by Fermat's principle and Snell's law. Due to the potentially large offsets for shallow scatterers, conventional Dix inversion is not suitable for correcting the air-layer effect (Pue et al., 2016). Consequentially, some authors have considered

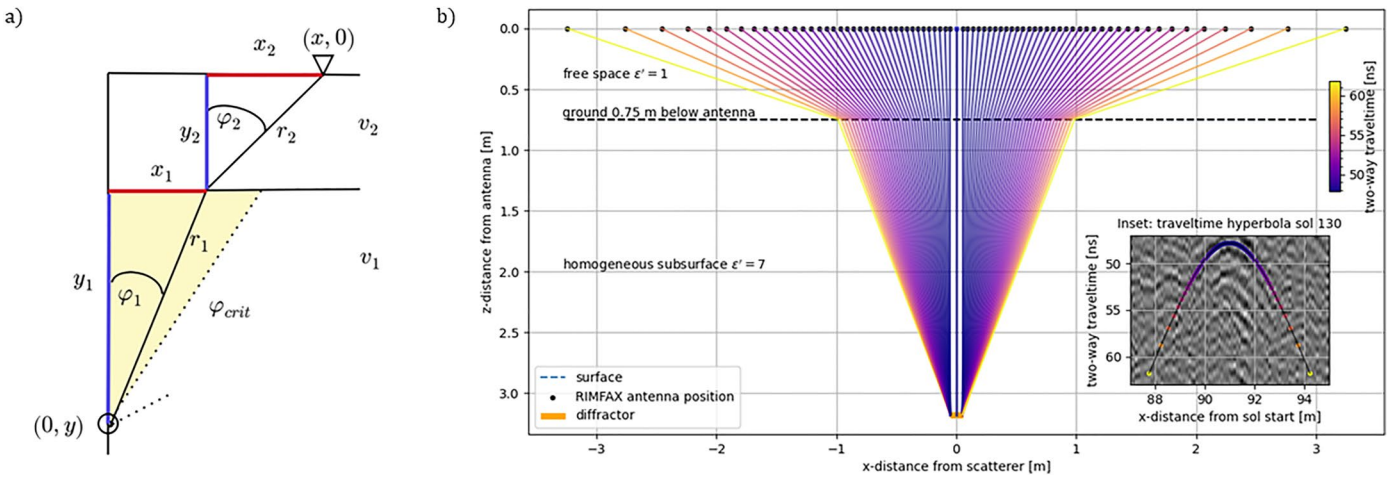

Figure 2. (a) Model with two layers, variables as in Equations 2–4. The antenna is positioned at $(x, 0)$ (triangle) and the point-like scatterer at $(0, y)$ (circle). Red and blue: horizontal and vertical path length in each layer. Yellow: Field of illumination in subsurface for $v_1 < v_2$. (b) Two-layered model for a subsurface permittivity of $\varepsilon' = 7$, free space permittivity $\varepsilon' = 1$, and a scatterer (diffractor) in 2.4 m below the surface. Inset: the resulting hyperbolic curve fits a hyperbolic pattern on sol 130.

surface refraction for Chang'E-4 data analysis (Fa, 2020; R. Wang et al., 2021), showing that a neglected surface refraction leads to an underestimation of the permittivity. For different subsurface models and a bistatic antenna, R. Wang et al. (2021) model the permittivity underestimation to range within 10%–50% in a depth of 1–4 m, with the homogeneous subsurface model and more shallow scatterers being most affected. Their antenna is modeled up to a height of 0.4 m, such that the 0.75 m high RIMFAX antenna would likely result in even stronger underestimation, despite the different monostatic configuration of RIMFAX.

In contrast to the classical hyperbola matching, we regard the free space under the antenna as one layer of a medium comprised of N homogeneous layers. The twt curve for the coherent reflection from a scatterer in a layered medium is then as follows:

$$t(x) = 2\sum_{i=1}^{N}\frac{r_i(x)}{v_i} = 2\sum_{i=1}^{N}\frac{\sqrt{x_i(x)^2 + y_i^2}}{v_i}, \tag{2}$$

with pathlength r_i in layer i, horizontal layer distance $x_i(x)$, layer height y_i, and layer velocity v_i, as in Figure 2a. The bottom layer is coincident with the scatterer depth.

Since the angle of incidence at the surface and therefore $x_i(x)$ is not known, this becomes a two-point ray tracing case through a stack of laterally infinite homogeneous layers without a closed form expression. However, we can regard the scatterer as a passive point source in depth with respect to the emerging wavefront from the scatterer (Bauer et al., 2019). Thus, we calculate the twt $t(\varphi)$ and antenna position $x(\varphi)$ for a radiation angle φ to the surface-normal as follows:

$$\begin{aligned} t(\varphi) &= 2\sum_{i=1}^{N}\frac{r_i(\varphi_i)}{v_i} \\ x(\varphi) &= \sum_{i=1}^{N}\sqrt{r_i^2 - y_i^2} \\ \varphi_i &= \arcsin\left(\frac{v_i}{v_{i-1}}\cdot\sin\varphi_{i-1}\right), \end{aligned} \tag{3}$$

with $r_i = y_i/\cos\varphi_i$, $x_i = \sqrt{r_i^2 - y_i^2}$, and $\varphi_1 = \varphi$. $t(\varphi)$ can be interpolated to a twt curve $t(x)$ and fitted to hyperbolic shapes in the data by adapting the layer velocities v_i. The layer height can be retrieved from the data-derived apex traveltime $t(0) = t_{apex}$ of the hyperbolic shape by

$$y_i = \left(\frac{t_{apex}}{2} - \sum_{j=1, j\neq i}^{N}\frac{y_j}{v_j}\right)v_i, \tag{4}$$

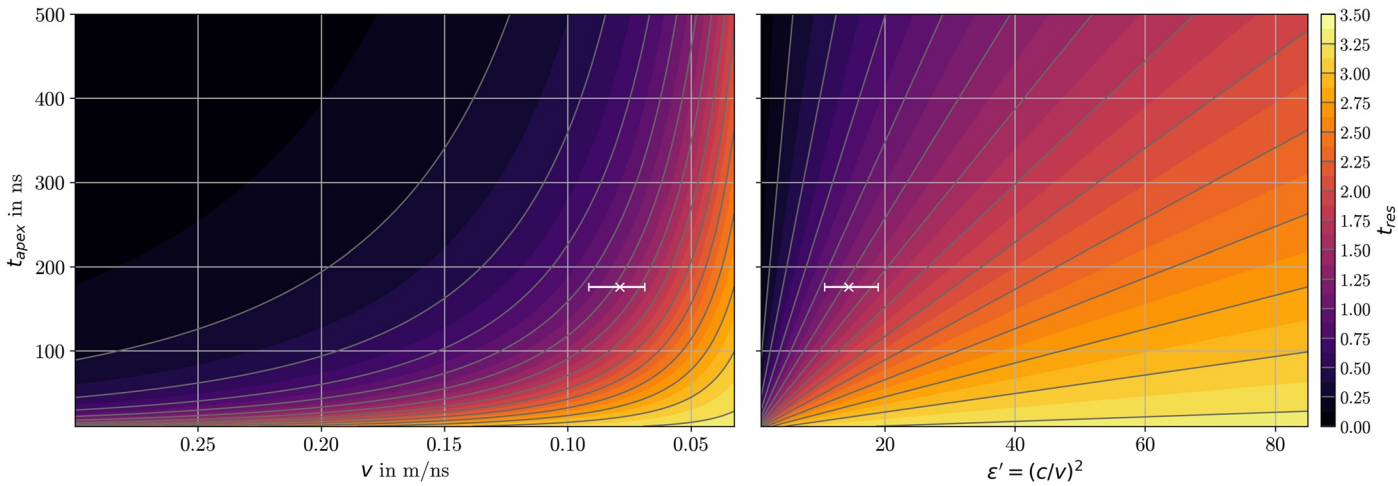

Figure 3. Uncertainty of the model for (a) v-t_{apex} and (b) ε'-t_{apex} parameter space. Color-coded residual twt $t_{res} = t(x) - t_{apex}$ at an offset of $x = 1$ m. t_{apex} subtracted from the twt to display the residual steepness. Gray lines are residual twt-isolines with 0.25 ns spacing and color spacing 0.125 ns. White: Example measurement with errorbar for a fitting uncertainty of 0.5 ns: Velocities (permittivities) within the errorbar lie within the uncertainty range.

given that all but one pair of y_j, v_j are known, such as in the case of the two-layer case of free space and subsurface. An example for this two-layer case as used for the data analysis in this study is displayed in Figure 2b: A scatterer is located 2.4 m below the surface and is 10 cm wide, (1/3 of the RIMFAX center wavelength) and is therefore considered a point-like object. The inset shows a hyperbolic shape in the data of sol 130, matched by the modeled hyperbolic curve for $\varepsilon' = 7$.

It is important to note that the surface refraction introduces a critical angle of reflection for the rays traveling back from the slower subsurface into Martian atmosphere at $\varphi_{crit} = \arcsin\left(1/\sqrt{\varepsilon'}\right)$. The field of illumination of the passive source is therefore constrained to a cone with narrowing opening angle 2φ for the two-layer case, see yellow area in Figure 2a. In practice this also means that scatterers can only be detected for smaller offsets from the apex position for lower velocities, since the ray density and therefore strength of the coherent signal at large offset positions is declining with increasing velocity contrast at the layer boundary.

2.2. Uncertainty of the Method

2.2.1. Quantification of Fitting Uncertainty

The uncertainty of the method can be quantified by analyzing the effect of a small traveltime change on the derived velocity. This traveltime variation can occur through ambiguous hyperbolic patterns in the data and the subsequent fitting uncertainty. The fitting for this study is done by visual inspection; however, the method uncertainty analysis also applies to an automated fitting procedure in a layered medium.

We assume a traveltime uncertainty of Δt, at the offset x for a measured velocity of v_1 for a hyperbola with apex-time t_{apex}. This will result in a velocity uncertainty of Δv_1 as in $\Delta v_1(\Delta t)|_{x,t_{apex},v_1}$. Theoretically, a large evaluation offset x leads to less uncertainty, since the hyperbolic branch is the steepest in the limit of infinite offset. However, the largest observable offset depends on the strength of the received scattered signal. In practice, the signal decays with offset, due to a nadir focused antenna beam pattern and the attenuation induced by off-nadir, longer travel paths. Thus we chose $x = 1$ m, at which many hyperbolic patterns still show coherent energy, see Figure S1. The remaining two parameters are v_1 and t_{apex}. We model the twt $t(x)$ with Equations 3 and 4 over the 2 dimensional parameter space v_1 and t_{apex}. We use cubic interpolation to retrieve the twt at the exact offset x. Figure 3 shows the residual twt $t_{res} = t(x) - t_{apex}$ for this parameter space, once for a v_1-axis (a) and once for a ε'-axis (b). To get t_{res}, we subtract t_{apex} from each $t(x)$ in order to give a measure of relative flatness, independently from the depth-dependent absolute twt. The parameter map can be interpreted as follows: We assume a Δt fitting uncertainty at offset $x = 1$ m and have a measurement at t_{apex} with fitting model velocity v_1. For the same t_{apex}, hyperbolas within Δt around the modeled $t(x)$ lie within the uncertainty range of the fit. A subsurface with those velocities is therefore within a Δt uncertainty range. In Figure 3, $\Delta t = 0.5$ ns equals one color segment left and right of any point.

In Figure 3a, the isolines grow closer to each other toward lower velocities or earlier times, when the respective other parameter is kept constant. An exception occurs in the lower right zone, where the spacing is enlarged again. Outside that zone, we observe that for constant permittivity or velocity, later scatterers experience a higher uncertainty range. This is consistent with hyperbolic flattening, a geometric effect of illuminating a scatterer from farther away, where the 1 m offset is too small to fall within the steep branch region of the hyperbolic pattern. Within the lower right zone, we observe the inverse effects yet much weaker. The uncertainty increases in the direction of lower velocities and of earlier scatterers. This can be attributed to the refraction occurring in the layered model. A significant portion of the ray path is then located in the top, high-velocity layer (free space) and only a small subsurface volume is sampled by the ray, since the critical angle steepens toward the vertical with higher velocity contrast. The scatterer depth simultaneously decreases for a constant t_{apex} in a slower medium, thus further increasing the uncertainty of the model. In Figure 3b, the same analysis is shown in the permittivity domain. Here, it can be observed that permittivities experience a strong uncertainty increase toward higher values. However, this is predominantly an effect of the nonlinear characteristic of Equation 1 used to substitute ε' for v in Equation 3.

2.2.2. Further Sources of Uncertainty

The frequency range of 150–1,200 MHz relates to a free space wavelength of 2–0.25 m, such that the uppermost part of the subsurface is in the near-field range for parts of the frequency spectrum. The subsurface geometry is inherently 3D, therefore reflection points can move outside the xy-plane. Scatterers located offtrack will appear deeper than their actual depth and the travel path estimates are less accurate. Generally, false positive detections of hyperbolic patterns cannot be ruled out. The shallow subsurface is considered to be homogeneous in permittivity, leading to average permittivity values. We opt to utilize the homogeneous model due to significant variations in stratigraphy (Hamran et al., 2022), a low number of scatterers relative to the distance covered, and the absence of evident permittivity clusters (see Section 3).

2.3. Conversion of Permittivity to Density

Within the literature, there exist a variety of permittivity-density formulas for different mixing models and different rock types, most notably the Apollo mission derived lunar regolith formula (Carrier III et al., 1991):

$$\varepsilon' = 1.91^{\rho}. \tag{5}$$

In a study of powdered regolith material, Hickson et al. (2018) find $\varepsilon' = 1.96^{\rho}$ using a Lichtenecker mixing model (LI), while listing a literature range of the constant from 1.85 to 2.15. For their preferred Looyenga-Landau-Lifshitz mixing model (LLL) for regolith, they find $\varepsilon' = (0.307\rho + 1)^3$. Rust et al. (1999) introduce a LI and a linear fit for their samples with $\varepsilon' = 2.22^{\rho}$ and $\varepsilon' = 2.26\rho + 1$, respectively. Their samples consist of dry volcanic rocks, excluding basalts. As an outlier in the range of constants, Shmulevich et al. (1971) measured even relatively higher permittivities, a LI fit to their 59 samples most relevant for the Jezero environment gives $\varepsilon' = 2.48^{\rho}$, and a LLL fit of $\varepsilon' = (0.47\rho + 1)^3$. Although information on their measurement and sample configuration is incomplete, it may suggest that using the constant 1.91 in the lunar regolith Equation 5 can lead to an overestimation of permittivity-derived densities for solid mafic rock in Jezero.

Due to specific experimental setups and samples, the formulas above do not cover the full spectrum of solid mafic rocks. Following F. T. Ulaby and Long (2014), we therefore use the midrange constant of 2.0 for this study and Equation 5 becomes

$$\varepsilon' = 2.0^{\rho}. \tag{6}$$

We note that the derived densities in this work are in the upper half of the density spectrum estimated from the literature constants for LI-mixing, while linear or LLL models tend to infer even higher densities for large permittivities due to their lesser slope.

3. Results

3.1. Data Acquisition and Processing

RIMFAX raw data are acquired as discussed in Hamran et al. (2020). For processing, we use a background removal, Blackman windowing per trace, and front zero-padding to remove the constant phase term as in

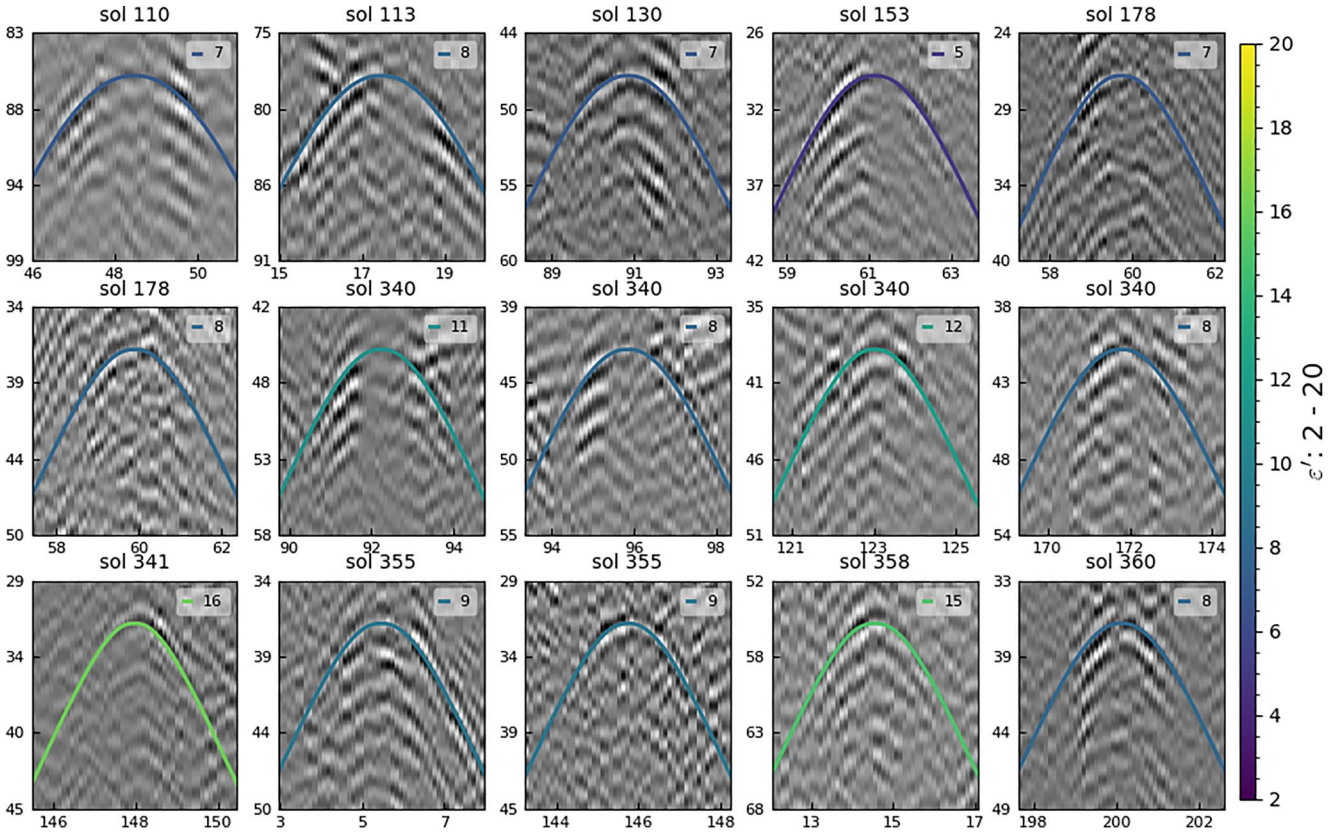

Figure 4. Scatterers along the traverse for large markers in Figure 5. x: distance from sol start in m. y: time from antenna feed point in ns. Patterns show varying degrees of shape impurities.

Eide, Casademont, Øyvind L. Aardal, and Hamran (2022). No topographic correction is applied since it is velocity-dependent. After Fourier transformation with tail zero-padding for interpolation and linear mapping to time domain, an attenuation compensation gain and time-cut to the antenna feed point at 19.4 ns is applied. The acquisition modes used for scatterer detection are "shallow" and "surface," since the "deep" mode rarely sees scatterers due to hyperbolic flattening and the strong signal decay of point reflectors as opposed to smooth flat reflection targets. The shallow mode uses the full 1,050 MHz bandwidth, has a sweep time of 6.25 milliseconds, 610 samples per sweep and stacking of 16 consecutive sweeps, and a gate frequency of 3.125 kHz. An adaptation to the shallow mode from sol 47 after early mission testing led to slightly higher gain in shallow reflections, including the surface. The soundings are recorded every 0.1 m based on rover wheel odometry, thus accounting for potential Rover velocity variations. However, the actual sounding-to-sounding odometric distance varies slightly, with a standard deviation of 0.01 m up to sol 379. We therefore average the sounding spacing per sol for the hyperbolic matching. Hyperbolic patterns during Rover turns are dismissed based on the rover positioning data, such that the traverse can be approximated as a straight line within a pattern aperture of 1–4 m.

3.2. Scatterers

A total of 150 patterns are considered for permittivity and density determination. Figure 4 shows the most prominent scattering patterns along the traverse, corresponding to the big markers in Figure 5 (for all patterns see Figure S1). The data patches are overlain by a matching hyperbola with permittivity ε', following the model in Section 2.1. The patterns are less well-defined than in conventional ground-coupled GPR. Some patterns have varying signal amplitude throughout the hyperbolic branches. The shape impurities and amplitude variation can be a consequence of nonideal scatterer geometries, the frequency-dependent antenna beam pattern, local coupling effects due to surface roughness, and antenna movement.

Figure 5 shows the scatterer distribution with permittivity along the full traverse in the first 379 sols of the mission. The traverse shows passages with scatterer clustering in the region around sol 113, 130, 155, and 171

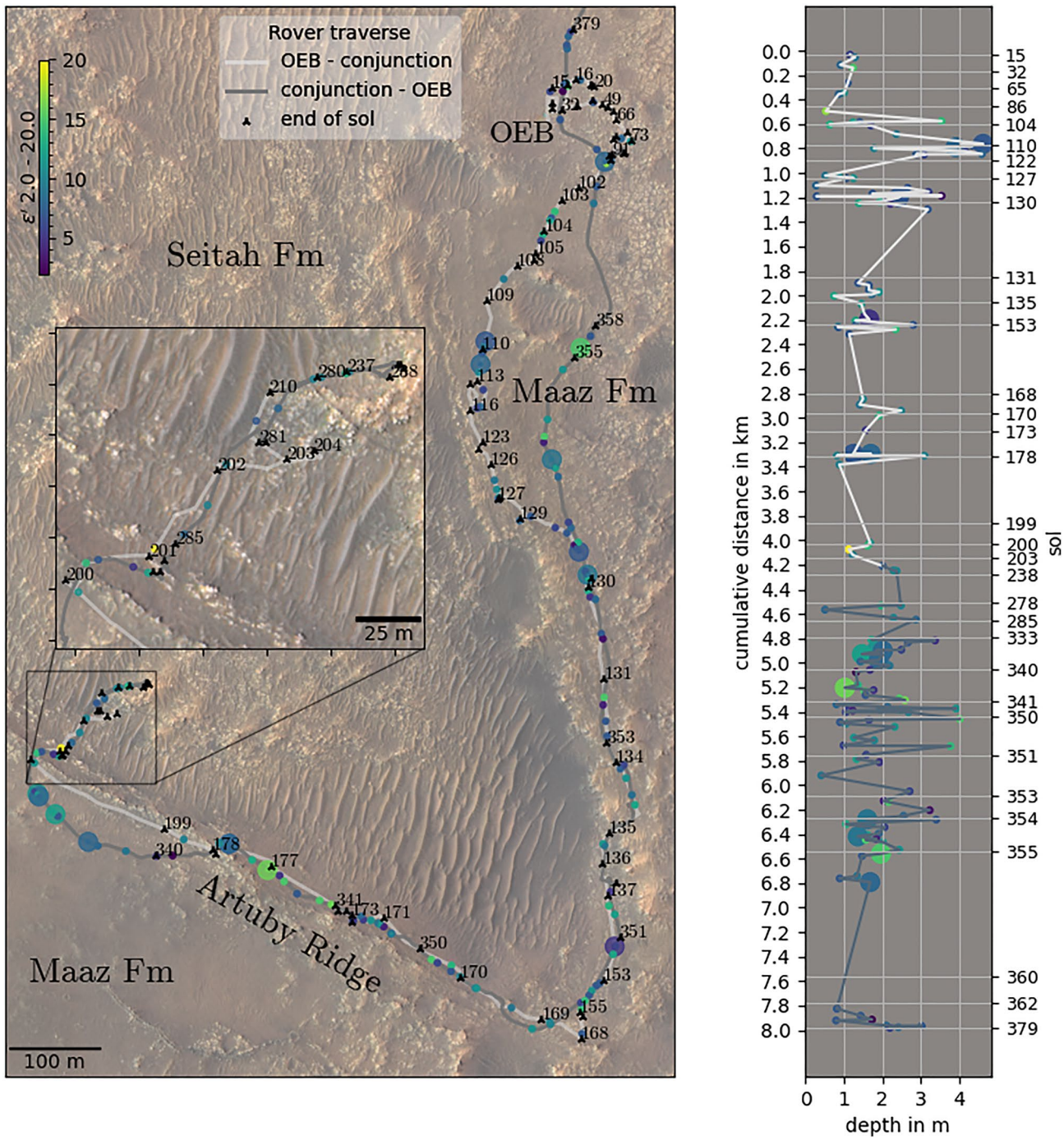

Figure 5. left: Rover traverse with permittivities along track for the route Octavia E. Butler landing site to the conjunction parking location in Séítah (sol 210) and back. Basemap: Mars 2020 Science Team RGB-colored HiRISE mosaic. Color-coded permittivity as in Figure 4. Big dots correspond to hyperbolas from Figure 4. Zoom: Séítah toe dip traverse. Right: Depth of scatterers along the traverse. The location of scatterers as well as permittivity and depth appear disorganized along the traverse.

and passages with few or no scatterers such as during sol 200 and 360. While the clusters correspond to a region close to the Séítah—upper Máaz or Séítah—lower Máaz boundary, sol 200 does not show scatterers. It follows the boundary closely but on top of the Artuby ridge instead of below. Deeper into Artuby on the return sol 340, more scatterers are observed again. The scatterer depth varies substantially within 1–3 m, a cluster deeper than 4 m depth is observable around sol 110 on the drive leg OEB—Séítah. These scatterers are in the vicinity of the

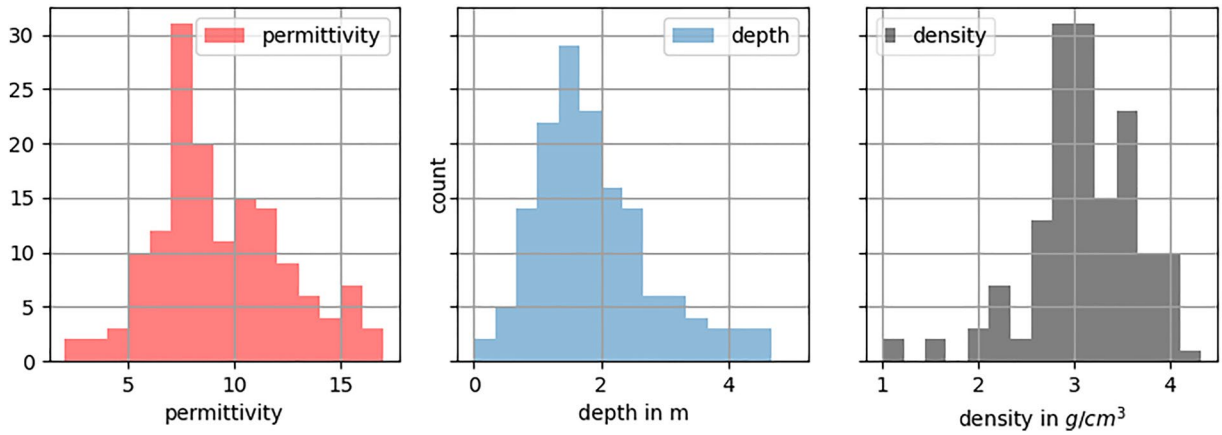

Figure 6. Permittivity, depth, and density histograms for all measurements. Density is derived from permittivity with Equation 6. Clustering can be observed around $\varepsilon' = 8$, depth 1.7 m, and density 3.0 g/cc, slightly skewed toward larger values.

Adziilii structure, an impact crater between end of drive sol 109 and sol 358. They could be related to a strongly disturbed subsurface from the impact; an in-depth study of this region is needed.

The absence of low-permittivity zones stretching over several 100 m sections of the traverse in Figure 5 indicates a homogeneous depositional environment such as a series of lava flows, lacking major depressions filled with regolith. Such zones could exist at depth but cannot be confirmed given a lack of observed scatterers that could indicate otherwise.

We analyze the measurements in the following as a statistical distribution of independent measurements in Jezero Crater floor. Figure 6 shows the permittivity, depth, and density histogram. All show distinct clustering around the median $\varepsilon' = 8$, depth 1.7 m, and density 3.0 g/cc. They appear slightly skewed toward higher permittivities, deeper scatterers, and higher densities.

Figure 7 shows the velocity-time and permittivity-time distribution. A general signature of high permittivities at later t_{apex} toward low permittivities at earlier times can be observed. This is consistent with increasing density with traveltime resulting from regolith to bedrock transitions and overburden-induced compaction. The scatterers accumulate in the 20–70 ns region, with a maximum apex time of 110 ns. This concentration could be attributed to a higher detection rate within this zone due to the restrictions for deep scatterers described in Section 2.1. The matching uncertainty background map shows that the highest permittivity samples experience a large matching

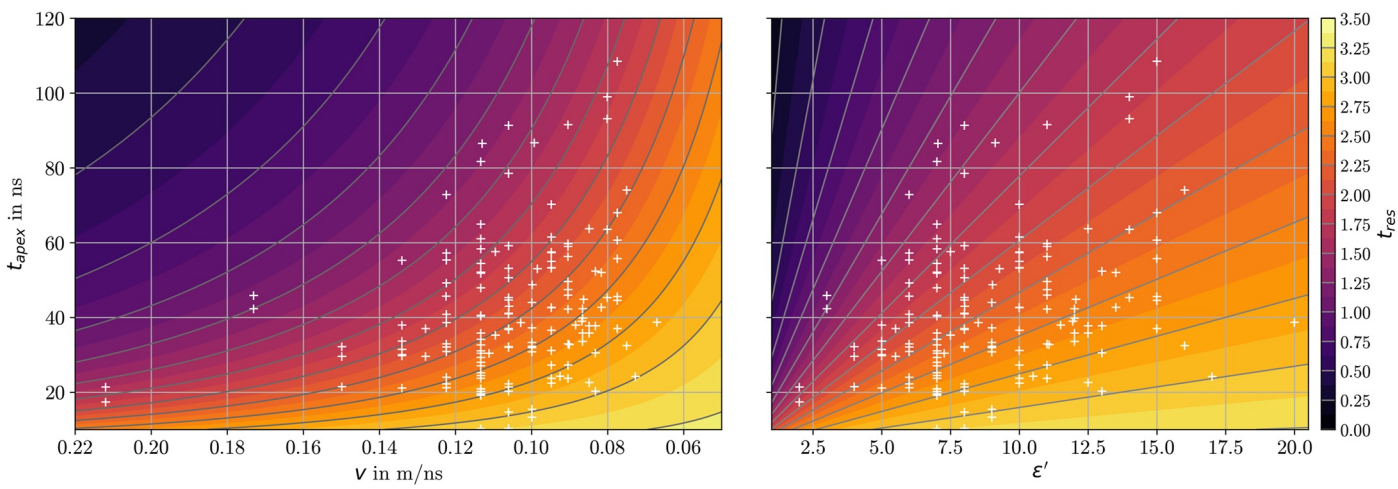

Figure 7. Permittivity (a) and velocity (b) to t_{apex} distribution of scatterers (white marks). Background colormap shows the model-based residual traveltime $t_{res} = t(x_0) - t_{apex}$ at offset $x = 1$ m with isolines spacing $\Delta t = 0.25$ ns and color spacing 0.125 ns, as in Figure 3. High permittivity values experience a stronger uncertainty, see also example in Figure 3. The scatterers are distributed toward slower velocities at later times, consistent with a density gradient in the subsurface.

Table 1
Statistical Properties of All 150 Samples, Rounded

	Apex time in ns	Permittivity	Velocity in m/ns	Density in g/cc	Depth in m
Median	37.9	8.0	0.11	3.0	1.7
Mean	41.1	8.9	0.10	3.1	1.9
σ	20.0	3.2	0.02	0.6	1.0

uncertainty, especially for early apex times. For the highest permittivity sample with $\varepsilon' = 20$ at $t_{apex} = 40$ ns, the range is approximately $12 < \varepsilon' < 39$. Alternatively, high permittivities could also be a result of high permittivity material such as magnetite (Dam et al., 2013) or hematite.

An overview of the all measurements is given in Table 1. With a median permittivity of 8.0 and density of 3.0 g/cc, we interpret the Martian subsurface within the upper 5 m to be predominantly solid bedrock. The permittivity is consistent with permittivities found in dry, basaltic lava flows on Earth (Campbell & Ulrichs, 1969; F. Ulaby et al., 1990), as well as with orbital radar derived values for lava flows on Mars (Carter, Campbell, Holt, et al., 2009; Shoemaker et al., 2022; Simon et al., 2014). We infer that the scattering structures are likely comprised of sharp edges or cavities within lava flow regimes. The scatterer are positioned both within flow units as well as between successive flow events on the erosional contrast.

3.3. Density Trend Along the Traverse

The density variation across the drive regions upper Máaz (east of Séítah), lower Máaz (south of Séítah), and Séítah is presented in Table 2. We observe a potential trend indicating an increase in median densities among these regions yet with significant statistical uncertainty. This could indicate that Séítah is on average denser than upper Máaz within the observed depth range. However, the exact formation boundaries are not known and, particularly the lower Máaz drive region is likely comprised of both Máaz and Séítah material in the sounded subsurface. We note, however, that all $\rho(\varepsilon')$-functions in Section 2.3 are monotonic and trend-conserving as such. Thus the observed trend is independent of the absolute density due to the selection of the mixing model and the underlying rock samples utilized in creating those functions.

4. Discussion

4.1. Cross-Instrument Comparison of Densities

The densities obtained by RIMFAX and the density difference between Máaz and Séítah compare well with the SuperCam density measurements on surfacing rocks: SuperCam obtained mean densities for upper Máaz, lower Máaz, and Séítah of 3.10, 3.27, and 3.37 g/cc with a standard deviation of 0.01–0.03 g/cc, respectively (Wiens et al., 2022), (called in there: Máaz, Artuby, Séítah).

The SuperCam densities were calculated along with the CIPW norms (Cross, Iddings, Pirsson, and Washington) from the major-element compositions by estimating theoretical fractions of end-member mineral compositions and determining their relative contributions to the overall density. The compositional standard errors of the mean were propagated to estimate maximum and minimum densities from maximum possible felsic or mafic extremes. These errors reflect precision, showing that the difference in density between the units as observed by SuperCam is statistically significant. RIMFAX densities are an average of a 3D subsurface volume and thus are inherently of higher uncertainty, in addition to the conversion-based uncertainty introduced by Equation 6. The densities we measure are based on the average of a volume of material below the surface. As a result, there is a higher degree of uncertainty in our measurements. This is in addition to the uncertainty introduced by the conversion process outlined in Section 2.3. SuperCam densities do not account for porosity, while RIMFAX densities are bulk rock densities. Porosity values along the traverse would enhance the comparability. However, since we do not have this information, we can only conclude that the radar density measurements are indicative of a subsurface that is at least moderately porous. Wiens et al. (2022) also observe that the higher up in the stratigraphic succession of Séítah, lower and upper Máaz, the higher the SiO2 and less the FeO + MgO content. X. Wang et al. (1999) show a negative correlation of permittivity (and hence density) with SiO2 and a positive correlation with metal-oxides, further linking the mineralogical trend with the RIMFAX permittivity measurements. Finally, the sol 173 rock target "Entreveaux" with Seitah composition (Wiens et al., 2022) shows the direct proximity of Máaz and Séítah material along the drive in the lower Máaz region.

Table 2
Densities of Subregions in g/cc, Rounded

	Upper Máaz (92 detections)	Lower Máaz (45)	Séítah (13)
Median	3.0	3.2	3.3
Mean	3.0	3.0	3.4
σ	0.6	0.6	0.4

Analyses of mineral chemistry and modal percentages (vol%) of surface rocks in Séítah by PIXL (Planetary Instrument for X-ray Lithochemistry)

provide a direct estimate of the bulk density. PIXL conducted multispectral images of two abraded patches and detailed X-ray fluorescence (XRF) analyses on one of them. The XRF raster maps span about 0.5 cm^2. Different mineral phases are identified based on chemistry in the scanned areas in the abraded patches. The identity of these minerals are consistent with those observed using the Raman method (Liu et al., 2022, and references therein). Using the correlation between minerals and their spectral responses, the mineral distribution of the whole patch can be estimated using the PIXL multispectral data. The density is calculated using the density for the specific mineral chemistry and the volume percentages and was found to be 3.33 ± 0.01 g/cc. Including the mineral alteration would still yield a density of 3.21 g/cc, such that this altered subsurface would still produce densities of the same magnitude in RIMFAX measurements. Like SuperCam, PIXL densities do not account for porosity yet the abraded patches show no higher degrees of such.

Given the method's increase in uncertainty with higher permittivities (or densities) as well as the limited scatterer count, we must interpret this Máaz-Séítah density trend strictly in conjunction with other data sets and observations. Namely, we use the stratigraphic observations of the Séítah-Máaz formation boundary made by Hamran et al. (2022) for sol 201, the comparable density trend observed by SuperCam, the highly localized but accurate Séítah density obtained by PIXL, and lastly the close proximity of Máaz and Séítah material (Entreveaux) in parts of the lower Máaz drive region. Thus, we support the interpretation that there exists a possible density trend, while the pure RIMFAX result, with hyperbola matching only, do not require a trend in the first 379 sols. A homogeneous subsurface interpretation is in-line with results from Eide, Casademont, Berger, et al. (2022), whose radar wave attenuation measurements demonstrate this across the first 379 sols.

4.2. Comparison to GPR Permittivity Results on the Moon

Rover-mounted GPRs have been used to investigate permittivity and density of the upper meters of the shallow Lunar subsurface by the Chinese Chang'E-3 and 4 missions, using a comparable methodology and similar GPR frequency spectrum (see Section 2). Chang'E-3 finds permittivities up to 3.8 in the first 120 ns and equivalent regolith densities of up to 2.1 g/cc by Equation 5 (Lai et al., 2016). The Chang'E-4 landing site is interpreted to be highly porous regolith of several meters in thickness (Lai et al., 2019; Li et al., 2020). The permittivity range is 2.5–4.5 with corresponding densities of 1.4–2.3 g/cc (Feng et al., 2022; Lai et al., 2019). Accordingly, most of the Lunar subsurface for which GPR derived density values exist is considered to be fine regolith. In contrast to that, the subsurface of the Jezero Crater floor as seen by RIMFAX is likely composed of mafic bed-rock structures reaching close to or are exposed at the surface.

5. Conclusion

The initial estimates of subsurface dielectric permittivity and bulk rock density in Jezero Crater from sol 15–379 support the interpretation of a subsurface comprised of dense, mafic material. These estimates were obtained using a hyperbola matching technique that employs a two-layer model of the Martian atmosphere and a homogeneous subsurface, accounting for surface refraction. The derived median permittivity of 8.0 and median density of 3.0 g/cc are consistent with values obtained from orbital radar and laboratory measurements of lava flows on Mars and Earth. The densities are also in line with the measurements obtained by the Rover instruments SuperCam and PIXL from surficial rocks. Detected scatterers along the traverse do not display distinct grouping by region, depth, or density. A potential exception is a higher density in Séítah than in upper Máaz and a transitional zone around lower Máaz. This trend, however, can only be sustained by a multi-instrument comparison. Future work aims to enhance the detection rate and robustness of the rock property determination, combined with surface-reflectivity based permittivity inversion. With a growing number of detections, the scatterer distribution can shed more light on structural subsurface changes along the Rover traverse.

Data Availability Statement

The data used in this work are available at the NASA PDS Geosciences Node (Hamran & Paige, 2021). The derived parameters from this study are available at https://github.com/Titus-Casademont/RFAX_crater_floor_velocity (Casademont et al., 2023).

Acknowledgments
The first author is funded by the Norwegian Research Council through the Grants 301238 and 309835. Contributions by YL and DCN were carried out at the Jet Propulsion Laboratory, California Institute of Technology, under a contract with the National Aeronautics and Space Administration 80NM0018D0004. We thank the RIMFAX team and R. C. Wiens for fruitful discussions, as well as the two anonymous reviewers.

References

Bauer, A., Schwarz, B., Werner, T., & Gajewski, D. (2019). Unsupervised event identification and tagging for diffraction focusing. *Geophysical Journal International*, *217*(3), 2165–2176. https://doi.org/10.1093/gji/ggz106

Campbell, M. J., & Ulrichs, J. (1969). Electrical properties of rocks and their significance for lunar radar observations. *Journal of Geophysical Research*, *74*(25), 5867–5881. https://doi.org/10.1029/JB074i025p05867

Carrier, III. W. D., Olhoeft, G. R., & Mendell, W. (1991). *Lunar sourcebook: A user's guide to the moon*. In G. H. Heiken, D. T. Vaniman, & B. M. French (Eds.), (pp. 475–594). Cambridge University Press. Retrieved from https://www.lpi.usra.edu/publications/books/lunar_sourcebook/

Carter, L. M., Campbell, B. A., Holt, J. W., Phillips, R. J., Putzig, N. E., Mattei, S., et al. (2009). Dielectric properties of lava flows west of Astraeus mons, Mars. *Geophysical Research Letters*, *36*(23), L23204. https://doi.org/10.1029/2009GL041234

Carter, L. M., Campbell, B. A., Watters, T. R., Phillips, R. J., Putzig, N. E., Safaeinili, A., et al. (2009). Shallow radar (SHARAD) sounding observations of the medusae fossae formation, Mars. *Icarus*, *199*(2), 295–302. https://doi.org/10.1016/j.icarus.2008.10.007

Casademont, T. M., Eide, S., Shoemaker, E. S., Liu, Y., Nunes, D. C., Dypvik, H., et al. (2023). RIMFAX ground penetrating radar reveals dielectric permittivity and rock density of shallow Martian subsurface [Dataset]. Zenodo. https://doi.org/10.5281/zenodo.7681150

Dam, R. L. V., Hendrickx, J. M. H., Cassidy, N. J., North, R. E., Dogan, M., & Borchers, B. (2013). Effects of magnetite on high-frequency ground-penetrating radar. *Geophysics*, *78*(5), H1–H11. https://doi.org/10.1190/GEO2012-0266.1

Dong, Z., Fang, G., Zhao, D., Zhou, B., Gao, Y., & Ji, Y. (2020). Dielectric properties of lunar subsurface materials. *Geophysical Research Letters*, *47*(22), e2020GL089264. https://doi.org/10.1029/2020GL089264

Dong, Z., Feng, X., Zhou, H., Liu, C., Zeng, Z., Li, J., & Liang, W. (2020). Properties analysis of lunar regolith at Chang'E-4 landing site based on 3D velocity spectrum of lunar penetrating radar. *Remote Sensing*, *12*(4), 629. https://doi.org/10.3390/rs12040629

Eide, S., Casademont, T., Aardal, Ø. L., & Hamran, S.-E. (2022). Modeling FMCW radar for subsurface analysis. *Ieee Journal of Selected Topics in Applied Earth Observations and Remote Sensing*, *1–1*, 2998–3007. https://doi.org/10.1109/JSTARS.2022.3165135

Eide, S., Casademont, T. M., Berger, T., Dypvik, H., Shoemaker, E. S., & Hamran, S.-E. (2022). Radar attenuation in the shallow Martian subsurface: RIMFAX time-frequency analysis and constant-q characterization over Jezero Crater floor. *Geophysical Research Letters*. https://doi.org/10.1029/2022GL101429

Fa, W. (2020). Bulk density of the lunar regolith at the Chang'E-3 landing site as estimated from lunar penetrating radar. *Earth and Space Science*, *7*(2), e2019EA000801. https://doi.org/10.1029/2019EA000801

Farley, K. A., Stack, K. M., Shuster, D. L., Horgan, B. H. N., Hurowitz, J. A., Tarnas, J. D., et al. (2022). Aqueously altered igneous rocks sampled on the floor of Jezero Crater, Mars. *Science*, *377*(6614). https://doi.org/10.1126/science.abo2196

Feng, J., Siegler, M. A., & White, M. N. (2022). Dielectric properties and stratigraphy of regolith in the lunar south pole-Aitken basin: Observations from the lunar penetrating radar. *Astronomy & Astrophysics*, *661*, A47. https://doi.org/10.1051/0004-6361/202143015

Feng, J., Su, Y., Ding, C., Xing, S., Dai, S., & Zou, Y. (2017). Dielectric properties estimation of the lunar regolith at CE-3 landing site using lunar penetrating radar data. *Icarus*, *284*, 424–430. https://doi.org/10.1016/j.icarus.2016.12.005

Ganesh, I., Carter, L. M., & Smith, I. B. (2020). SHARAD mapping of arsia mons caldera. *Journal of Volcanology and Geothermal Research*, *390*, 106748. https://doi.org/10.1016/j.jvolgeores.2019.106748

Hamran, S.-E., & Paige, D. A. (2021). Mars 2020 rimfax bundle. PDS. NASA planetary data system. https://doi.org/10.17189/1522644

Hamran, S.-E., Paige, D. A., Allwood, A., Amundsen, H. E. F., Berger, T., Brovoll, S., et al. (2022). Ground penetrating radar observations of subsurface structures in the floor of Jezero Crater, Mars. *Science Advances*, *8*(34). https://doi.org/10.1126/sciadv.abp8564

Hamran, S.-E., Paige, D. A., Amundsen, H. E. F., Berger, T., Brovoll, S., Carter, L., et al. (2020). Radar imager for Mars' subsurface experiment—RIMFAX. *Space Science Reviews*, *216*(8), 128. https://doi.org/10.1007/s11214-020-00740-4

Hickson, D., Boivin, A., Daly, M. G., Ghent, R., Nolan, M. C., Tait, K., et al. (2018). Near surface bulk density estimates of NEAs from radar observations and permittivity measurements of powdered geologic material. *Icarus*, *306*, 16–24. https://doi.org/10.1016/j.icarus.2018.01.018

Horgan, B., Udry, A., Rice, M., Alwmark, S., Amundsen, H., Bell, J., et al. (2022). Mineralogy, morphology, and emplacement history of the Maaz formation on the Jezero crater floor from orbital and rover observations. *ESS Open Archive*. https://doi.org/10.1002/essoar.10512674.1

Lai, J., Xu, Y., Zhang, X., & Tang, Z. (2016). Structural analysis of lunar subsurface with Chang'E-3 lunar penetrating radar. *Planetary and Space Science*, *120*, 96–102. https://doi.org/10.1016/j.pss.2015.10.014

Lai, J., Xu, Y., Zhang, X., Xiao, L., Yan, Q., Meng, X., et al. (2019). Comparison of dielectric properties and structure of lunar regolith at Chang'E-3 and Chang'E-4 landing sites revealed by ground-penetrating radar. *Geophysical Research Letters*, *46*(22), 12783–12793. https://doi.org/10.1029/2019GL084458

Li, C., Su, Y., Pettinelli, E., Xing, S., Ding, C., Liu, J., et al. (2020). The Moon's farside shallow subsurface structure unveiled by Chang'e-4 lunar penetrating radar. *Science Advances*, *6*(9). https://doi.org/10.1126/sciadv.aay6898

Li, C., & Zhang, J. (2021). Velocity analysis using separated diffractions for lunar penetrating radar obtained by yutu-2 rover. *Remote Sensing*, *13*(7), 1387. https://doi.org/10.3390/rs13071387

Liu, Y., Tice, M. M., Schmidt, M. E., Treiman, A. H., Kizovski, T. V., Hurowitz, J. A., et al. (2022). An olivine cumulate outcrop on the floor of Jezero Crater, Mars. *Science*, *377*(6614), 1513–1519. https://doi.org/10.1126/science.abo2756

Pue, J. D., Meirvenne, M. V., & Cornelis, W. M. (2016). Accounting for surface refraction in velocity semblance analysis with air-coupled GPR. *Ieee Journal of Selected Topics in Applied Earth Observations and Remote Sensing*, *9*(1), 60–73. https://doi.org/10.1109/JSTARS.2015.2439333

Rust, A., Russell, J., & Knight, R. (1999). Dielectric constant as a predictor of porosity in dry volcanic rocks. *Journal of Volcanology and Geothermal Research*, *91*(1), 79–96. https://doi.org/10.1016/S0377-0273(99)00055-4

Schwarz, B. (2019). An introduction to seismic diffraction. In C. Schmelzbach (Ed.), *Advances in geophysics* (pp. 1–64). Elsevier. https://doi.org/10.1016/bs.agph.2019.05.001

Shmulevich, S. A., Troitskiy, V. S., Zelinskaya, M. R., Markov, M. S., & Sukhanov, A. L. (1971). Dielectric properties of rocks at a frequency of 500 mhz. *Earth Physics*, (12), 68–76. (translated by Adam Peiperl).

Shoemaker, E. S., Carter, L. M., Garry, W. B., Morgan, G. A., & Plaut, J. J. (2022). New insights into subsurface stratigraphy northwest of ascraeus mons, Mars, using the SHARAD and MARSIS radar sounders. *Journal of Geophysical Research: Planets*, *127*(6), e2022JE007210. https://doi.org/10.1029/2022JE007210

Simon, M. N., Carter, L. M., Campbell, B. A., Phillips, R. J., & Mattei, S. (2014). Studies of lava flows in the tharsis region of Mars using SHARAD. *Journal of Geophysical Research: Planets*, *119*(11), 2291–2299. https://doi.org/10.1002/2014JE004666

Stillman, D., & Olhoeft, G. (2008). Frequency and temperature dependence in electromagnetic properties of Martian analog minerals. *Journal of Geophysical Research*, *113*(E9), E09005. https://doi.org/10.1029/2007JE002977

Udry, A., Ostwald, A., Sautter, V., Cousin, A., Beyssac, O., Forni, O., et al. (2022). A Mars 2020 iPerseverance/i SuperCam perspective on the igneous nature of the Máaz formation at Jezero Crater and link with Séítah, Mars. *Journal of Geophysical Research: Planets*. https://doi.org/10.1029/2022je007440

Ulaby, F., Bengal, T., Dobson, M., East, J., Garvin, J., & Evans, D. (1990). Microwave dielectric properties of dry rocks. *IEEE Transactions on Geoscience and Remote Sensing*, *28*(3), 325–336. https://doi.org/10.1109/36.54359

Ulaby, F. T., & Long, D. G. (2014). *Microwave radar and radiometric remote sensing*. The University of Michigan Press.

Wang, R., Su, Y., Ding, C., Dai, S., Liu, C., Zhang, Z., et al. (2021). A novel approach for permittivity estimation of lunar regolith using the lunar penetrating radar onboard Chang'E-4 rover. *Remote Sensing*, *13*(18), 3679. https://doi.org/10.3390/rs13183679

Wang, X., Guo, H., Wang, C., Chen, P., & Shi, Y. (1999). Relative dielectric constant from dry rocks. *Chinese Science Bulletin*, *44*(24), 2286–2293. https://doi.org/10.1007/BF02885941

Watters, T. R., Campbell, B., Carter, L., Leuschen, C. J., Plaut, J. J., Picardi, G., et al. (2007). Radar sounding of the medusae fossae formation Mars: Equatorial ice or dry, low-density deposits? *Science*, *318*(5853), 1125–1128. https://doi.org/10.1126/science.1148112

Wiens, R. C., Udry, A., Beyssac, O., Quantin-Nataf, C., Mangold, N., Cousin, A., et al. (2022). Compositionally and density stratified igneous terrain in Jezero Crater, Mars. *Science Advances*, *8*(34). https://doi.org/10.1126/sciadv.abo3399

Erratum

In the originally published version of this article, the first paragraph in the conclusion, beginning with "The initial estimates of subsurface" and ending with "investigation using multiple instruments" was incorrectly added. The paragraph has been removed, and this version may be considered the authoritative version of record.